Salt Concentration Dependence of the Mechanical Properties of $LiPF_6$/Poly(Propylene Glycol) Acrylate Electrolyte at a Graphitic Carbon Interface: A Reactive Molecular Dynamics Study

Osvalds Verners,[1] Alexey V. Lyulin,[3] Angelo Simone[1,2]

[1]Faculty of Civil Engineering and Geosciences, Delft University of Technology, Delft, The Netherlands
[2]Department of Industrial Engineering, University of Padova, Padua, Italy
[3]Group Theory of Polymers and Soft Matter, Department of Applied Physics, Eindhoven University of Technology, Eindhoven, The Netherlands
Correspondence to: O. Verners (E-mail: o.verners@tudelft.nl)

Received 30 October 2017; accepted 2 January 2018; published online 8 March 2018
DOI: 10.1002/polb.24584

ABSTRACT: This reactive molecular dynamics study explores the salt concentration dependence of the viscoelastic and mechanical failure properties of a poly(propylene glycol)/$LiPF_6$-based solid polymer electrolyte (SPE) at a graphitic carbon electrode interface. To account for the finite-size effect of interface-confined SPE films, the properties of two distinct film thicknesses are compared with the respective bulk properties. Additionally, the effect of uniaxial compression in the interface-normal direction on free energy profiles of Li-ion SPE-desolvation is studied. © 2018 The Authors. Journal of Polymer Science Part B: Polymer Physics Published by Wiley Periodicals, Inc. J. Polym. Sci., Part B: Polym. Phys. **2018**, *56*, 718–730

KEYWORDS: failure properties; molecular dynamics; solid polymer electrolyte; viscoelastic properties

INTRODUCTION Structural batteries are considered as a promising design solution for mobile, electricity-powered devices, and vehicles.[1,2] The concept consists in integrating the energy storage elements into structural elements to achieve a reduction in total weight and volume of the devices. Multifunctional applications also pose additional challenges due to different and possibly conflicting requirements for optimum performance with respect to both functionalities. To address these issues, this contribution investigates the dependence on salt concentration of the mechanical properties of an interface between a graphitic carbon (GC)-based electrode and a poly (propylene glycol) acrylate (PPGDA)[3]-based solid polymer electrolyte (SPE). In structural terms, the interface represents a fiber/SPE-coating interface if a negative electrode is considered.[4]

An appealing approach for implementing a structural battery has been found in three-dimensional (3-D) battery architectures.[4] The approach offers advantages with respect to reduction of ionic-transport distance, which is significant for solid state batteries,[1] and the possibility of fiber/matrix type architectures,[5] which are advantageous for structural applications. Considering multifunctional applications, detailed knowledge about electrochemical and mechanical properties of applicable production materials and their interfaces is instrumental for the design of devices with optimum performance. However, to the best of our knowledge, previous computational studies on analogous composite structures of confined polymer or SPE films[6–11] have not considered both electrochemical and mechanical properties of the same material. In particular, the salt-dopant concentration effect on the mechanical properties of an SPE/electrode interface has not been considered explicitly at nanoscale.

A number of studies have been devoted to the mechanical behavior of surface-grafted polymers, including effects related to interfacial bond density[8] and polymer chain lengths.[9,12] Although the latter studies do not consider the effect of ionic dopants on interfacial chemo-adhesion properties, we regard their findings as applicable to this contribution since we view surface-grafting as structurally equivalent to the chemical bonding between SPE and GC substrate. We also note that, due to the employment of periodic chains and reactive force field-based

Additional Supporting Information may be found in the online version of this article.

method of interfacial bond generation (see the section "Methods"), the effects of bond density and polymer chain lengths are not investigated explicitly in this contribution. Furthermore, we mention that an investigation of chemical or thermal stability of the SPE is not considered in the present contribution either. The choice is justified by the close similarity of the chemical structure of PEO, which has been investigated with regard to the respective properties, and poly(propylene glycol) diacrylate (PPGDA), which is studied in the present contribution (see the section "SPE Unit Cell"). To this end, we refer to the results of a reactive MD study,[13] according to which an artificial, chemically-bonded interface (SEI) layer of PEO effectively prevents the co-intercalation of organic solvents into graphite and provides significantly better thermal stability than physically coated polymers. Likewise, an experimental study[14] reports reduced gel-polymer-electrolyte passivation and improved electrochemical performance, achieved by depositing a cross-linked SPE layer on the surface of a Li electrode. Further, we refer to a reactive MD study on PEO,[15] according to which a polymer that is confined between pristine graphene nanoplatelets shows a higher thermal stability compared to the bulk polymer, whereas an opposite effect is observed for graphene oxide nanoplatelets.

Multiple studies[6,10,11] have been devoted to the study of adhesive failure at solid substrate/polymer interfaces that we regard as the structural analogue for the structures considered in this contribution prior to forming chemical bonding across the interface. However, as our simulations indicate negligible shear resistance for such adhesive interfaces, the structures without chemical interface bonds were not considered for further mechanical study. Nonetheless, we would like to mention several studies which have considered improvement of adhesion strength by application of functional groups on a graphitic surface. According to a study using static molecular mechanics,[7] mild oxidation enhances interfacial adhesion between graphene (representing carbon fiber), and organic polymers. The findings indicate a qualitative agreement with an experimental study[16] that reports improved interfacial-shear strength of carbon fiber with plasma-grafted polyurethane coating compared to carbon fiber with acid-anhydride-grafted sizing. The improvement is attributed to a significant increase in oxygen-containing groups. To theoretically assess the potential improvement of cohesive properties of nonbonded interfaces, selected O-containing groups for surface termination will be considered for comparison in the section "Effect of Surface Termination on Adhesion Properties."

According to refs. 17,18, and this study, the interaction between the polymer matrix and $Li(PF_6)_n$ ($n \geq 1$) ion groups consists in concentration-dependent clustering of salt ions. As the ion/polymer interactions may be considered as a small scale limit of nanoparticle/polymer interactions, we refer to a possible interpretation for phenomena which occur as a result of nanoparticle/matrix interactions,[19] obtained using generic MD simulations. According to the study, the viscoelastic properties of polymer–nanoparticle composites (PNCs) are independent of particle size and can be described as a product of the respective property of a polymer matrix (dynamic shear modulus or viscosity) and a function of particle volume fraction (eqs 6 and 7, respectively, in ref. 19). In particular, the viscoelastic stiffness is found to be dependent on the dominant type of interaction (attraction, neutrality, or repulsion) between nanoparticles and the polymer. Consequently, the findings are seen as a theoretic explanation for experimentally observed correlation between salt concentration and SPE stiffness[20] and will be addressed further in context of the viscoelastic properties of the SPE in the section "Viscoelastic Properties and Ion Coordination."

Last, we would like to mention the findings of a coarse-grained MD study on generic cross-linked, interface-confined-polymer films[21] according to which polymer-chain ordering in the normal direction of the interface is critically dependent on the smoothness of the confining surface. In particular, an amorphous surface has been reported to significantly reduce the chain ordering and the polymer density (adhesion) at the interface compared to smooth and rough crystalline surfaces. The applicability of the findings for interpreting the effect of surface in the currently studied structures will be addressed in the section "SPE Structure."

Consequently, the aim of this contribution is to determine the optimum $LiPF_6$ salt concentration with respect to reversible deformation limits and shear-induced damage mechanisms. This knowledge facilitates an evaluation of the material's safety against a loss of structural performance due to interfacial debonding. To this end, a chemically bonded interface is considered for the study of the failure properties of interface-parallel shear. In particular, failure strain, failure stress, bond-dissociation damage, and damage localization dependence on $LiPF_6$ concentration are considered in the section "Mechanical Failure in Thin-Film SPE." Thereby, the contribution is regarded as an application and extension of existing knowledge of mechanical properties of interfaces, consisting of grafted polymeric materials and a solid substrate, to multifunctional applications as structural battery components. Additionally, the dependence of the free energy profile of Li ions during migration across the interface in uniaxial compression state, with deformation along the interface normal, is studied in the section "Li Migration in Compressed State."

METHODS

Structures

For all structures, except for the shear deformed (see the section "Simulation Settings and Ancillary Simulation Results") and open surface structures (see the sections "Graphitic Carbon/SPE Interface" and "Structures for Adsorption Energy Calculations"), periodic boundary conditions were used.

SPE Unit Cell

The periodic unit cell of a cross-linked SPE consists of a mixture of periodic segments of poly(propylene glycol) (PPG) and propylene glycol diacrylate (PGDA) cross-linker molecules. To generate the cross-links, the carbon atoms of the methyl group

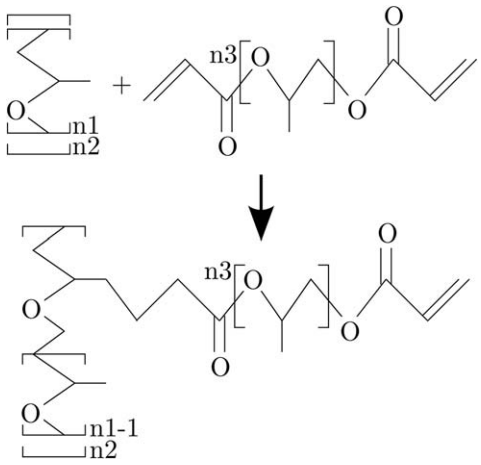

FIGURE 1 Cross-linking reaction of PPG and PGDA molecules, where $n1$ is the number of monomer units that form the backbone molecules, $n2$ is the number of monomer units that form the backbone segment between two consecutive cross-linking sites, and $n3$ is the number of monomer units that form the cross-linker molecules. Here, $n1=\infty$ (due to periodicity), $n2=2$, $n3=1$.

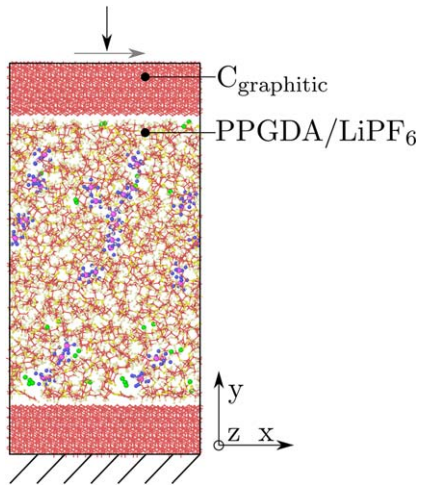

FIGURE 3 Loading modes (gray arrows represent interface-parallel/*yx*-direction shear; black arrows represent interface-normal/*y*-direction uniaxial compression) shown on a load-free sample configuration of a 60-Å-thick SPE/graphitic carbon film structure (C ●, H ●, O ●, Li ●, P ●, F ●). [Color figure can be viewed at wileyonlinelibrary.com]

branches of the PPG backbone were bonded with the terminal (C–C double bond) carbon atoms of the PGDA-cross-linker acrylate groups (Fig. 1) yielding EO:CO = 3:1 (EO represents ether-oxygen atoms, CO represents carbonyl-oxygen atoms), four backbone-segment replicas per unit cell, and eight propylene-glycol units per backbone segment. Due to the particular cross-link layout, the two directions that are orthogonal to the periodic backbone direction (z) were deemed most suitable for representing the behavior of an isotropic bulk material. Thereby, a cross-linking level of 50% with respect to the total number of PPG-methyl-group/PGDA-terminal-C cross-linking sites in the system was obtained (Fig. 2). Non-cross-linked SPE structures were not considered in this contribution.

Confined Film and Bulk SPE Structures

Given the structural battery context of this contribution, its main focus is therefore on the interface and the adjacent material structure between a GC-based electrode and PPGDA- (poly(propylene glycol) diacrylate)[3] and $LiPF_6$-based SPE (Fig. 3).

To estimate the effect of the thickness in confined SPE films, the SPE unit cell (see the section "SPE Unit Cell") was used to obtain two film thicknesses (Fig. 4) by replication. Additionally, for the estimation of ion distribution in the 60-Å-thick SPE film, structures with enlarged interfacial area of approximately 64×53 Å^2 were produced for the salt concentrations of Li:O = 1:48/1:24/1:16.

For a comparison with bulk properties, which can be related to conditions of infinite film thickness, periodic, cross-linked PPG structures with an approximate size of $40\times40\times30$ Å^3 were produced. Here we note that, due to the periodic definition of cross-linked polymer chains (see the section "SPE Unit Cell"), only the number of one-dimensionally periodic chains, each represented by a periodic segment consisting of 16 propylene-glycol units, could be established.

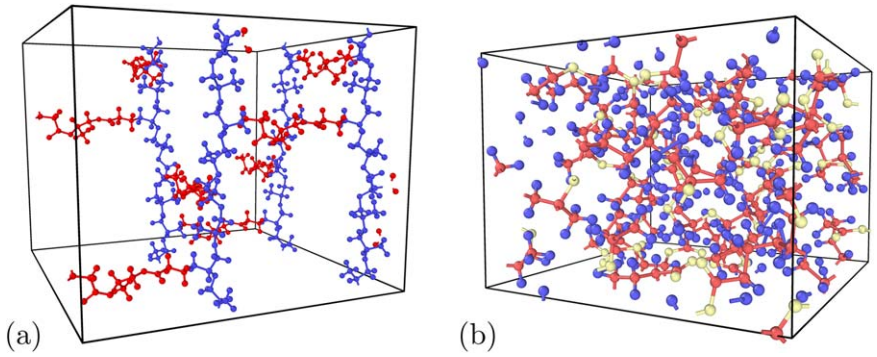

FIGURE 2 Configurations of 50%-cross-linked PPG unit cells: (a) 0 K, low density (0.2 g/cm^3; ● backbone atoms, ● cross-links) and (b) 300 K, 1 atm equilibrated (520 atoms; C ●, H ●, O ●). [Color figure can be viewed at wileyonlinelibrary.com]

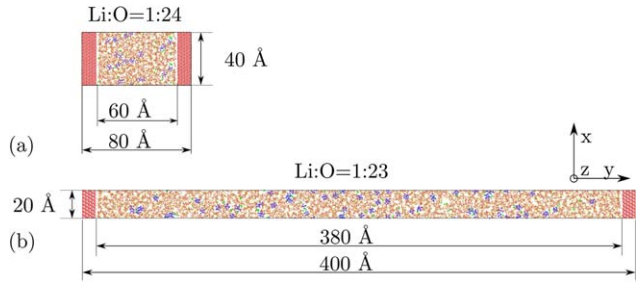

FIGURE 4 Dimensions of the SPE/graphitic–carbon film structures for (a) 60-Å- and (b) 380-Å-thick SPE films, shown at the same scale (*z*-dimensions are 25 Å and 27 Å, respectively). [Color figure can be viewed at wileyonlinelibrary.com]

The size of the segment is determined by the assumed degree of cross-linking with respect to PPG monomers (50%, with one cross-link per two units), yielding eight units for a repetitive element with four 90°-separated cross-links [Fig. 2(a)]. The expansion level of two, yielding 16 units per segment, was determined as sufficient in a previous study.[22] Thereby, 24/76/16 periodic PPG molecules with PPGDDA cross-links were obtained for the 60-Å-/380-Å-thick film and bulk SPE structures, respectively.

$LiPF_6$ was selected as an example of a common salt used in Li-ion battery electrolytes, studied computationally,[17,18] and implementable in terms of the available MD potentials (see the section "Simulation Settings and Ancillary Simulation Results"). The choice is subject to validity of the assumption that the salt effect on thermal stability of interface and solid–electrolyte interface (SEI) forming reactions is not posing significant additional constraints. Here it should be noted that, considering the hydrophobic properties of the studied polymer,[23,24] the findings of an experimental study comparing the electrochemical stability of hydrophobic and hydrophilic electrolytes[25] suggest that water contamination effects for the studied SPE should not be significant.

$LiPF_6$ molecules at Li:O ratios (O represents the oxygen atoms of the polymer unit cell) of 1:96/1:48/1:32/1:24/1:16 were added to the 60-Å-thick SPE film prior to equilibration. Here we indicate that, due to $LiPF_6$ concentration-dependent changes of volume, the thickness of the 60 Å SPE film is given as the mean value for the considered concentration range (with a maximum of $\approx$ 18% volume expansion in film thickness direction for Li:O = 1:16 SPE with respect to the neat polymer film).

Due to computational limitations, only the single reference concentration of Li:O = 1:23, which approximately corresponds to that used in the experimental reference material,[3] was used for the largest film thickness (380 Å). The bulk structures were doped with $LiPF_6$ at concentrations of Li:O = 1:21/1:42/1:63/1:84. In the remainder of this contribution, the Li concentration in SPE structures is designated as x in Li:O = 1:24/x, unless noted otherwise, to emphasize the relation to experiment-compatible reference concentration.

Graphitic Carbon/SPE Interface

For the representation of a structural, electron-conductive component of a composite electrode, a 20-Å-thick GC (graphitic carbon) substrate with zigzag surface $(10\bar{1}0)$ was constructed. Due to the used cutoff (10 Å) for nonbonded interactions, the substrate thickness is considered sufficient to prevent SPE chain interactions through the film. The GC surface was considered as the reference plane ($y = 0$) for all spatial analysis plots. As Li staging phenomena[26,27] were not considered in this contribution, no initial lithiation of the GC structure was performed.

For an estimation of the shear-slip-related profile of bond damage (expressed as area-normalized bond count), applicable to fiber/matrix interaction modeling at continuum scale,[28] a structure with chemically bonded interface was used as described in the section "Simulation Settings and Ancillary Simulation Results." For all the other confined-SPE-film calculations, no chemical interfacial bonding was introduced, and, subsequently, Coulomb and van der Waals forces account for the interfacial interactions between GC and SPE. To maintain a structural similarity between structures with and without interfacial bonding, no surface-terminating functional groups were deposited on the GC surface.

Structures for Adsorption Energy Calculations

As an evaluation of surface termination effects, the adsorption energies of a PGDA molecule [Fig. 5(a)] and a 6-unit periodic segment of PPG [Fig. 5(b)] were calculated for a 13-Å-thick amorphous carbon film with a surface area of 16 $\times$ 18 $Å^2$. The two molecules correspond to the limit cases of a single-unit oligomer and periodic (infinite) polymer chain, respectively. For comparison, pure-C_{sp1}, $O_{carbonyl}$, and OH terminations, the latter two corresponding to possible functional groups of oxidized graphene,[29] were considered.

Simulation Settings and Ancillary Simulation Results

The simulations were performed using the MD package LAMMPS[30] with the USER-REAXC module.[31] To account for charge polarization effects during ion migration and study, the bond dissociation failure behavior resulting from the shear deformation of a chemically bonded interface, the reactive, empirical MD-potential ReaxFF,[32] with a parameter set that describes C/H/P/F/O/S/Li interactions, was used. The potential includes charge equilibration as proposed by Rappe and Goddard[33] and has been previously applied to organic–liquid–electrolyte[34,35] and SPE systems.[22] In ref. 22, the potential has been tested against density functional theory (DFT) with regard to nonbonded, elastic, and failure properties of single-chain PGDA oligomer and monomer molecules of different lengths and its capability to reproduce PEO dynamic viscosity. We point out that, according to a comparison of results of a test simulation of PEO/$LiPF_6$ SPE, described in Ref. 22, and experimental findings,[36] the degree of $LiPF_6$ molecule dissociation (fraction of free PF_6^- ions is 0.06 at 15 wt % $LiPF_6$ during simulation and 0.59 at 10 wt % $LiPF_6$ during experiment) is considered as notably underestimated by the potential. Consequently, an

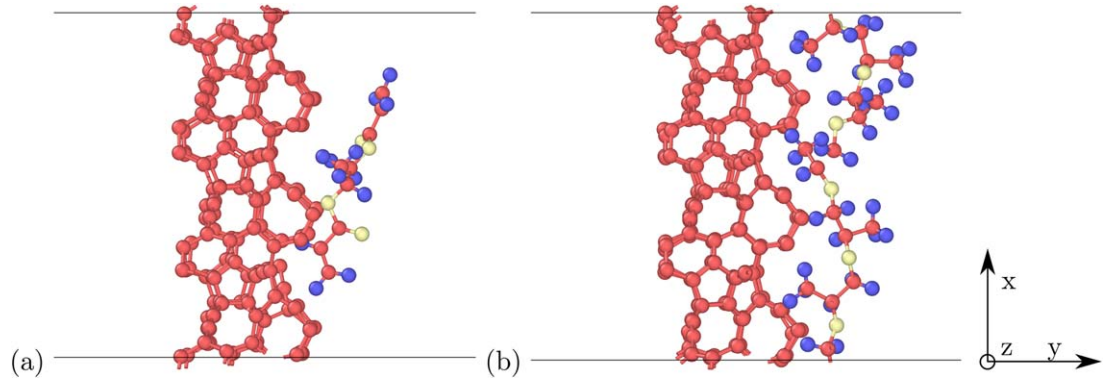

FIGURE 5 Sample configurations of (a) propylene glycol diacrylate and (b) 6-unit periodic poly(propylene glycol) polymer molecules on the surface of an amorphous carbon film (the surface is oriented perpendicular to the *y*-direction; C ●, H ●, O ●). [Color figure can be viewed at wileyonlinelibrary.com]

overestimate of ion clustering/aggregation is expected also in PPGDA SPE simulations. However, as no salt crystallization is observed and homogenizable mechanical properties are of main interest for this study, the above differences are not considered critical.

The simulations were performed under constant volume/temperature (NVT) ensemble conditions at 300 K applying the Nosé-Hoover thermostat, unless noted otherwise. The volume was fixed at the last equilibrium state of the prior constant pressure/temperature (NPT) equilibration run.

Undeformed State Simulations

The structures were initially energy minimized using a conjugate gradient (CG) method (max. force convergence criterion of 1e-6 kcal/mol/Å) combined with quadratic linesearch (max. displacement of 0.01 Å per outer iteration).[37] Minimization was stopped if the linesearch parameter $\alpha = 0$ or a maximum number of 1000 CG iterations was reached. The MD simulations were performed using Verlet type time integration[38] with a 0.25 fs time step.

For the creation of GC-substrate-compatible cell sizes, SPE films of low mass density (0.2 g/cm^3) were deformed over 250 ps, using quasi-static NVT ensemble conditions (300 K, Langevin thermostat with damping constant 25 fs), to the desired interface dimensions prior to SPE/GC structure assembly. Here we stress that the size of the SPE target cell was chosen to be compatible with an equivalent, NPT-equilibrated size of the bulk cell. For the creation of additional 60 Å-SPE-film structures (see the section "Confined Film and Bulk SPE Structures"), the same approach was used also in the direction normal to interface. The approach was justified by the considerations that only ion distribution, which was verified not to be significantly affected by the approach, was of interest and significantly longer NPT-equilibration times were typically observed for larger SPE structures. For bulk cells, the low-density structure [Fig. 2(a)] was used as the initial configuration for NPT equilibration. The rest of equilibration procedure is analogous for all SPE structures.

To obtain equilibrium states of condensed phase SPE at 300 K/1 atm, simulations were performed with a Nosé-Hoover barostat, coupled with five chain thermostats for pressure equilibration,[37,39] and a Langevin type thermostat for temperature equilibration.[37] LAMMPS-equivalent temperature-damping and pressure-damping constants of 25 and 250 fs, respectively, were used. Anisotropic pressure equilibration was applied by using a separate barostat for each orthogonal coordinate-axis direction.[37] After a condensed phase mass density of ≈ 1 g/cm^3 was reached, the Langevin thermostat was replaced with a Nosé–Hoover thermostat, consisting of three chain thermostats,[37,40] also with a damping constant of 25 fs, to complete the NPT ensemble equilibration. The pressure equilibration was considered complete when convergence with respect to the system's mass density in terms of a local maximum was reached. Simialrly, a subsequent NVT-ensemble equilibration was considered complete when a local minimum of potential energy was observed. Approximate minimum time for identifying a local extremum with respect to both parameters was of at least 0.1 ns, after an equilibration time of up to 1 ns. If an assumed local energy minimum was proven to be unstable during a subsequent production run, the procedure was repeated until a next local minimum was reached.

The chemical bonding of the SPE/GC interface was performed under static (0 K) conditions by a uniform displacement of the pre-equilibrated SPE film by 1.5 Å toward the contact surface of the GC substrate, followed by energy minimization. No evident dependence of changes in C—C or C—O_{ether} bond ratio or absolute count on Li concentration could be discerned. Furthermore, the invariance of the total number in bonds, except for a slight reduction at $x = 1.5$, indicates no significant change in the total coordination number of atoms at the interface.

Calculations of the glass transition temperature T_g were performed for bulk and confined SPEs to enable comparison and serve as a reference for analyzing the rest of results. For calculation of T_g, a heating/cooling rate of $dT/dt = 1.2$ K/ps was applied under NPT ensemble conditions of 1 atm

(Nosé-Hoover barostat coupled with a Langevin thermostat). Due to the finite heating/cooling rate, a hysteresis effect was observed for the respective responses of density against temperature, resulting in effective T_g differences. Therefore, the mean of both responses was used to estimate the equilibrium state density at each temperature (Supporting Information, Fig. S1). We also point out that at ~600 K, polymer dissociation was observed to occur; therefore, the temperature range for T_g estimation was limited to the upper bound of 500 K. A comparison of the obtained mass density of 1.15 g/cm^3 for bulk-SPE with 1.17 g/cm^3 for pure PPGDA suggests a small decrease due to $LiPF_6$ doping. Consequently, a lower T_g of bulk SPE ($\approx$ 200 K) compared to pure PPGDA ($\approx$ 320 K, experimental reference $\approx$ 310 K[41] for $M_c = 188$ g/mol, $n = 2$) is considered as a result of a reduction in mass density. However, we point out that, due to noticeable differences in mass density being present only in temperature ranges $T < 150$ K and $T > 400$ K, the nonlinear temperature dependence of mass density in the operational temperature range of a battery is not considered as significantly affected by salt concentration. Last, we note that the obtained PPGDA density values indicate an overestimation compared to the experimental reference for PPGDA (1.065 g/cm^3,[42] MW = $\approx$ 800 g/mol). According to a comparison with DFT results,[22] the difference is related to stronger nonbonded interactions combined with weaker bonded interactions.

For the calculation of PGDA/PPG-molecule adsorption energies on an amorphous carbon surface, energy minimization was performed for 14 sample configurations of each type of adsorbed molecule (see the section "Structures for Adsorption Energy Calculations"). The sample configurations were extracted from 38 ps equilibrium simulations under NPT ensemble conditions (300 K, 1 atm) using the Langevin thermostat and Nosé-Hoover barostat (100 ps temperature and 25 ps pressure damping constants, respectively).

Deformed State Simulations

For the NVT simulations of shear deformation parallel to the interface (Fig. 3), 10-Å-thick terminal layers of substrate and SPE film, with all layer atoms fixed, were displaced with respect to each other at a velocity of 100 m/s (corresponds to 12–13 ns^{-1} strain rate depending on the salt concentration). The choice of the strain rate was determined exclusively by the capability of the computational resources and is compatible with rates that have been used in simulations of similar type.[6,8] As the fixed SPE layer represents a nonperiodic boundary condition in the direction of interface normal (y), the layer is considered as a means for reducing the effect of finite thickness of the film. Furthermore, we point out that, according to a previous study,[22] no bond failure was observed for the currently studied cross-linked SPE in hydrostatic compression up to 10 GPa. Consequently, the tensile strain component is considered as the principal strain component in shear and tension that may cause physical- or chemical-bonding failure in the currently studied and similar SPEs.

For an evaluation of free-energy changes due to Li ion migration across the interface, the respective PMF was estimated as a function of ion distance from the interface plane at different states of uniaxial compression normal to the interface. The choice of compressed state instead of shear-deformed state is motivated by the assumption that in volume-preserving shear the average free volume that is available for ion diffusion does not change. Compressed configurations ($\varepsilon = -0.05/-0.1$) were obtained by imposing a strain rate of 3 ps^{-1} under fixed lateral dimension conditions, as shown in Figure 3, and subsequently equilibrated under NVT ensemble conditions. Here we emphasize that the compression levels correspond to the range of lithiation induced expansion of graphitic carbon (6–10%, where lowest value corresponds to the initial lithiation stage)[26] and amorphous carbon (10–17%, site dependent).[27] For PMF calculations according to the thermodynamic integration formalism,[43] an incremental harmonic-bias potential, implemented as a part of the COLVARS module in LAMMPS,[44] was used with the nonlinear coupling relation

$$V(x) = 1/2k(x - x_0)^2, \tag{1}$$

where V is the bias potential, x is the collective variable with reference value of x_0, and the force constant

$$k = k_0 + \lambda^{\alpha}(k_1 - k_0), \lambda \in [0, 1], \tag{2}$$

where k_0, k_1, α are the parameters and λ is the coupling parameter. According to ref. 44, when the initial value of the force constant is zero, $\alpha > 1$ distributes the effects of introducing the restraint more smoothly over time than a linear dependence and ensures that there is no singularity in the derivative of the restraint free energy with respect to λ. For 40 bias force increments with subsequent 10 ps equilibration, parameter values $\alpha = 4$, $k_0 = 0$, $k_1 = 500$ kcal/mol were used for SPE-desolvation simulations.[37] The parameter values were adjusted empirically by comparing the smoothness of resulting bias energy change with respect to time. In particular, the parameter k_1 was minimized so that the target location of the Li ions would be reached within the chosen simulation time, starting from bias-free state according to $k_0 = 0$ setting. Constant mean–displacement–velocities of 0.45 and 0.35 Å/ps were imposed on Li ions in interface-normal direction during the desolvation simulations, respectively. The simulation time for deformation and PMF estimation simulations above can be derived from the provided rates and total strains/displacements, respectively.

Sampling, Analysis, and Postprocessing Methods

For an evaluation of the $LiPF_6$-concentration dependence of the viscoelastic responses of SPE structures, the instantaneous relaxation modulus of shear stress (ISRM), defined as $G(t=0)$, was estimated as a function of the shear stress autocorrelation (SSAC)[19]

$$G(t) = \frac{V}{k_B T} \langle P_{\alpha\beta}(t) P_{\alpha\beta}(0) \rangle, \tag{3}$$

where V is the volume, k_B is the Boltzmann constant, T is the temperature, and $P_{\alpha\beta}(t)$ are the off-diagonal (shear)

components of the instantaneous stress tensor of the structure.

The NPT ensemble was used for the respective production runs. Considering the estimated Rouse time for entangled PEO melts as being of order 100 ns,[45] linear curve fit ISRM approximations for a 25 ps sample time, estimated according to

$$G(t=0) \approx \frac{1}{t}\int_0^t G(t')dt', \tag{4}$$

were considered appropriate. We also mention that the employed sampling time corresponds to the minimum timescale for obtaining consistent $G(t)$ estimates (time integrals shown in Supporting Information, Fig. S2) based on the time integral of shear stress autocorrelation (eq 3) and its corresponding Einstein relation[19]

$$G(t)=\frac{V}{2k_BT}\frac{\partial}{\partial t}\left[\left\langle\left[\int_0^t P_{\alpha\beta}(t')dt'\right]^2\right\rangle\right]. \tag{5}$$

A single production run of at least 100 ps at each salt concentration was performed with a stress sampling frequency of 2.5 fs. For $G(t)$ calculations, a sliding-window-averaging algorithm[43] and 10 sampling sets per simulation, each equal to 50% of the sampling run, were used. We point out that due to a varying number of samples for each sampling-time value, $G(t)$ values up to about 60% of the maximum sampling time were considered for analysis.

For the estimates of PMF change during Li-ion SPE-desolvation, at least 14 sample trajectories were produced for each compression strain level (see the section "Deformed State Simulations"). For shear failure property estimates, 18 (salt-free structure) or 9 (others) sample trajectories with randomized distributions of initial velocities were used. We note that, due to single sampling trajectory being used at each respective salt concentration for the estimation of equilibrium state properties, including mass density, dynamic viscosity, and ion distribution, dispersion-related scatter is expected to be present in the respective data.

The standard errors of averaged quantities were calculated for a 95% probability interval assuming the normal (for adsorption energies, ISRM, and PMF) or Student (for shear failure properties) distribution. For structure visualization, the OVITO software was used.[46]

For a nanoscale interpretation of the macroscopic property results, ion complexation and coordination structure comparisons were performed by applying radial distribution and derived analyses. Specifically, time-averaged radial distribution functions (RDF) $g(r)$ and radial integrals of RDFs (IRDF) Int($g(r)$) were computed using a radial sampling-bin size of 0.1 Å. Atom or ion coordination was defined as the first neighbor Int($g(r)$) value for the respective atom or ion pair. In particular, the PF_6 ion coordination was identified with the P-atom coordination due to symmetry of the anion.

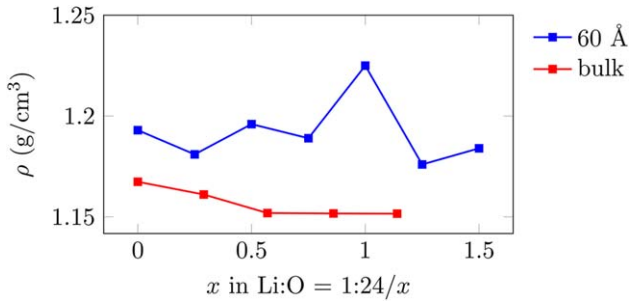

FIGURE 6 Dependence of the mean mass density of 60-Å-thick film and bulk SPEs on $LiPF_6$ concentration. [Color figure can be viewed at wileyonlinelibrary.com]

With the assumption that the contributions of pressure and entropy terms can be considered negligible at the simulations conditions (300 K, 1 atm), the solvation energy of $LiPF_6$ molecules in PPGDA was estimated as

$$E_{LiPF_6\ \text{solvation}}=(E_{SPE}-E_{PPGDA})/n-E_{LiPF_6}, \tag{6}$$

where E_{SPE}, E_{LiPF_6}, and E_{PPGDA} are the potential energies of the respective species in amorphous phase, and n is the number of $LiPF_6$ molecules in the system.

We note that the step of discretized property distributions (e.g., Figs. 8 and 9 and Supporting Information, Fig. S4) was chosen by the consideration of a minimum step size which would yield results that are unaffected by atomic scale inhomogeneities.

RESULTS AND DISCUSSION

SPE Structure

Except for an increase in mean mass density for the 60-Å-thick SPE film at $x = 1$ (discussed below), no significant effect due to change in salt concentration is observed (Fig. 6). Moreover, considering a monotonic reduction of mass density against increasing SPE-film thickness at an experiment-compatible salt concentration ($1.22 \pm 0.02/1.17 \pm 0.00/1.15 \pm 0.00$ g/cm^3 for the 60/380-Å-thick film and bulk SPEs, respectively, at Li:O≈1:23), an inverse correlation between SPE film thickness and mass density is assumed. The relation is attributed to interface confinement effects. Here we note that an earlier, coarse-grained MD study on interface confinement effects of a cross-linked generic polymer[21] reports no significant density change in the bulk-like part of the polymer film for different film thicknesses. The difference is interpreted as a result of the polymer being in a rubber-like state (reference study) instead of a glass/rubber transition state ($T_g \approx 280$ K at $x = 1$ according to Supporting Information, Fig. S1). Here we point out that the obtained mass density for the 60-Å-thick SPE film at $x = 1$ corresponds to the glassy state density in bulk SPE (≈ 1.9 g/cm^3 according to Supporting Information, Fig. S1). Consequently, due to the increased density, a more pronounced effect of inertia on failure localization closer to the displaced SPE layer (Fig. 3) is expected, as the peak value in Figure 7(b) suggests. However, due to being notably larger than those of sample structures at other concentrations, the density value is considered to be

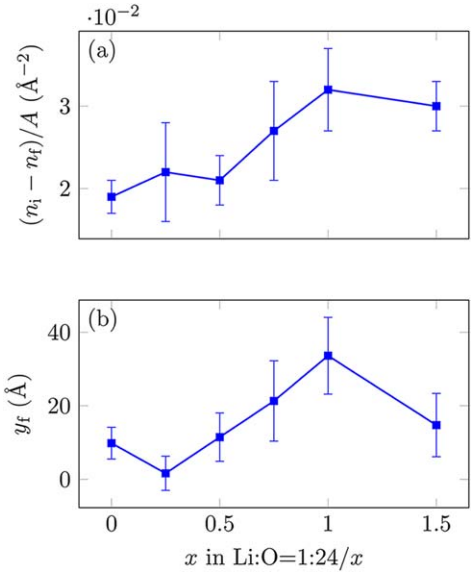

FIGURE 7 Dependence of (a) C—O_{ether} bond failure in shear (n_i is the initial number of bonds, n_f is the number of bonds after failure, A is the interface area, bond order cutoff = 0.3), and (b) failure location distance from the interface plane on $LiPF_6$ concentration ($y = 0$ Å) for the 60-Å-thick SPE film. [Color figure can be viewed at wileyonlinelibrary.com]

affected by dispersion in sample properties. The conclusion is supported by the NPT equilibration responses of density of structures with enlarged interfacial area (Supporting Information, Fig. S3), which indicate only a subtle increase with respect to salt concentration. We note that the initial density drop in Supporting Information, Figure S3 is due to the prior NVT compression from initial states of low density (see the section "Undeformed State Simulations").

Furthermore, considering the small reduction of mass density at the interface (Supporting Information, Figure S4), the interface role as a preferential site of glassy region nucleation, observed in structurally similar systems,[47] is not confirmed for the presently studied structures. Considering that the corrugated zigzag termination of GC represents an amorphous material surface, the result is found to be in a qualitative agreement with the study[21] in terms of the reduction of interfacial polymer density at amorphous confining surfaces.

For the 60-Å-thick SPE film at concentrations $x > 0.5$, ion segregation in form of a double layer is observed at $y < 10$ Å considering an increased Li-ion concentration at $y \approx 2$ Å and an increased PF_6 ion concentration at $y \approx 7$ Å (Fig. 8). The existence of the double layer is attributed to the formation of a charged GC layer at the interface (Supporting Information, Fig. S5). No direct comparison with the 380-Å-thick electrolyte could be established due to the absence of ions at $y < 20$ Å [Fig. 9(a)]. However, for both SPE film thicknesses, a small increase in PF_6 ion concentration towards the slab center was observed at compatible concentrations [Fig. 9(a) and 1:24/1:16 concentrations in Fig. 8(a,b)]. Considering the ion diffusion that would result from a similar gradient in PF_6

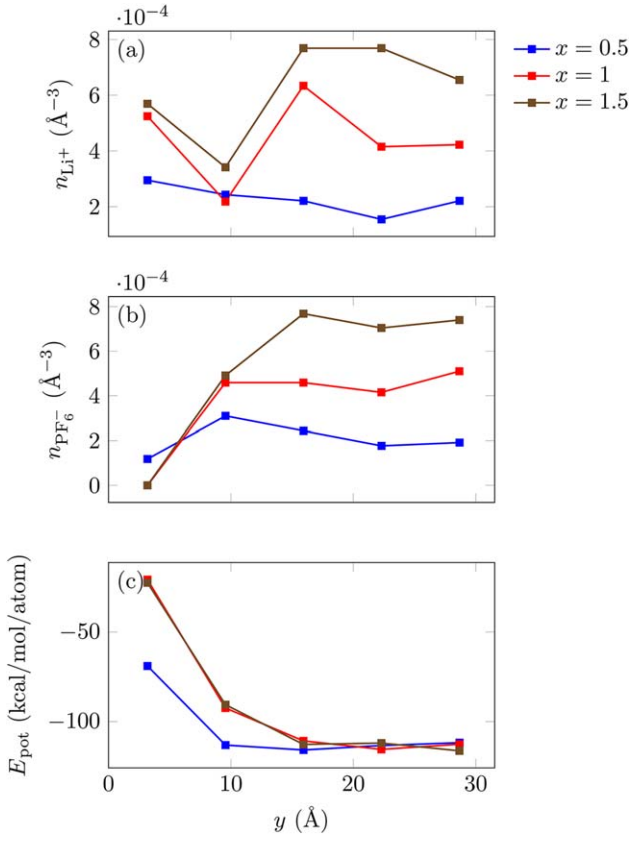

FIGURE 8 Dependence of (a) Li^+ and (b) PF_6^- ion number density and (c) $LiPF_6$ potential energy distribution across 60-Å-thick SPE films (3400 $Å^2$ interfacial area samples, $y = 0$ corresponds to the GC surface) on $LiPF_6$ concentration (expressed as x in Li:O = 1:24/x). [Color figure can be viewed at wileyonlinelibrary.com]

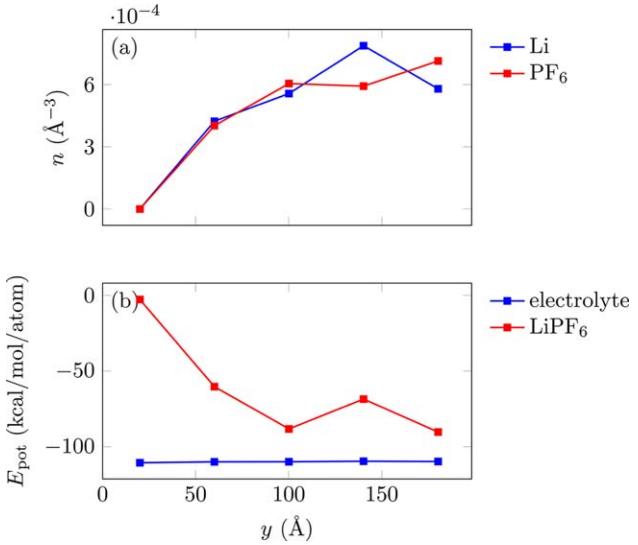

FIGURE 9 Distribution of $LiPF_6$ ion (a) number density and (b) potential energy across the 380-Å-thick SPE film (Li:O = 1:23, $y = 0$ corresponds to the GC surface). [Color figure can be viewed at wileyonlinelibrary.com]

TABLE 1 Adsorption energies (kcal/mol) of PPG (six periodic units) and PGDA molecules on a C_{amorph} surface for $C_{sp1}/O_{carbonyl}$/OH surface terminations (1 kcal/mol = 4.184 kJ/mol)

Termination	PPG	PGDA	(PPG + PGDA)/2
C_{sp1}	25.5 ± 0.7	16.4 ± 0.5	21.0
OH	40 ± 3	47 ± 1	43.2
$O_{carbonyl}$	59 ± 1	30.5 ± 0.5	44.9

ion concentration in bulk material, ion clustering effects (see the section "Viscoelastic Properties and Ion Coordination) and interface confinement are considered to account for the observed ion distribution. For Li ions, a similar trend was observed for the 380-Å-thick SPE film. However, for the 60-Å-thick SPE film, only at maximum salt concentration ($x = 1.5$) a compatible localization preference at $y > 10$ Å could be distinguished. The latter difference is explained by the observation that only at $x \geq 1$, an approximately constant Li concentration in the electric double layer was present. Last we add that, due to the nonuniform distribution of potential energy of Li and PF_6 ions [Figs. 8(c) and 9(b)], characterized by lowest energy at maximum concentration, and the insignificant dependence of solvation energy of $LiPF_6$ in bulk PPGDA on salt concentration at $x > 0.25$ (-16 ± 1 kcal/mol), inhomogeneous salt distribution in the vicinity of interface is regarded as an energetically favorable, thickness-dependent property in the considered range of concentration.

Effect of Surface Termination on Adhesion Properties

A comparison of adsorption energies for selected terminations of amorphous carbon (Table 1) indicates that the strongest interactions are those between $O_{carbonyl}$/PPG and OH/PGDA. However, mean values for each termination with respect to PPG/PGDA allow us to conclude that the surface of oxidized graphitic material may yield ≈ 50% higher interaction energy compared to neat (sp1-hybridized) carbon. The differences in energies are attributed to an enhancement of van der Waals type interactions due to the higher electronegativity of O compared to C.

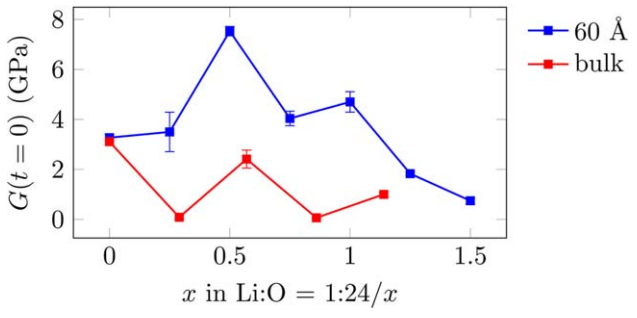

FIGURE 10 Dependence of ISRM on $LiPF_6$ concentration for the 60-Å-thick film against bulk SPEs. [Color figure can be viewed at wileyonlinelibrary.com]

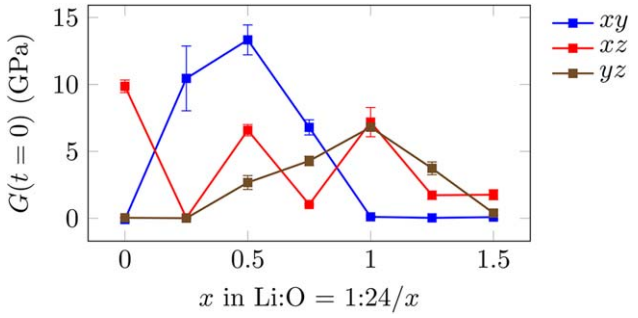

FIGURE 11 Dependence of ISRM components on $LiPF_6$ concentration for the 60-Å-thick SPE film. [Color figure can be viewed at wileyonlinelibrary.com]

Here we point out that according to an ab initio computational study,[48] oxidative terminations are expected to increase diffusive-intercalation-energy barriers for Li ions due to Li atom being trapped at the oxidative edge of graphite. In contrast, hydroxylic termination is found to lower the insertion barrier height at the step. Consequently, the adhesion energies of $O_{carbonyl}$/PPG and OH/PGDA terminations being similar, our preference for electrode applications is the OH-group termination.

Viscoelastic Properties and Ion Coordination

A test calculation indicates a cell size dependence of the ISRM of bulk SPE (Supporting Information, Fig. S6). The dependence is primarily attributed to the periodic topology of the unit cell (see the section "SPE Unit Cell"). Consequently, a quantitative ISRM comparison was performed only for the evaluation of salt concentration effect in SPE film structures of compatible thickness.

Similar to the bulk response,[22] configuration-dependent local anisotropy was observed due to the lack of evident trend with respect to maximum ISRM components (xy and yz) for the 60-Å-thick SPE film (Fig. 11). Furthermore, the highest ISRM values ($x = 0.5; 1$) were observed to coincide with the highest anisotropy between the components.

A significant increase in ISRM of the 60-Å-thin film against the bulk value in the concentration range up to $x \approx 1$ is observed (Fig. 10). The peak value at $x = 0.5$, however, is assumed to be subject to the dispersion in sample data. Similarly, the locally oscillatory pattern of both responses is attributed primarily to the data dispersion due to a single independent sample trajectory being used at each salt concentration (see the section "Sampling, Analysis, and Postprocessing Methods"). Consequently, only the differences in mean ISRM values and the concentration dependent changes in ISRM values that exceed the data oscillation amplitudes are considered for comparison. These are attributed to corresponding differences in mass density, T_g (see the section "SPE Structure"), and ion coordination (discussed below). Component-wise the distinction is attributed to the nonmonotonic responses of the xy and yz components (Fig. 11) that correspond to shear planes normal to the interface. In

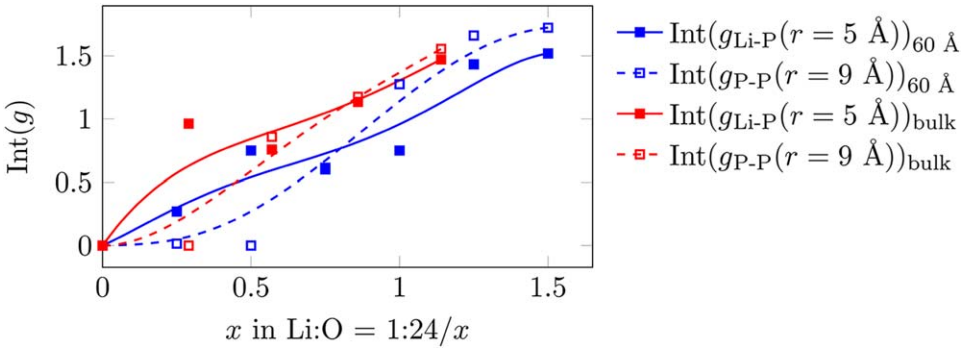

FIGURE 12 Dependence of Li-P/P-P first neighbor coordination shells on $LiPF_6$ concentration for 60-Å-thick film and bulk SPEs. [Color figure can be viewed at wileyonlinelibrary.com]

contrast, the response of the *xz* component is considered as qualitatively similar to the bulk response (Figs. 10 and 11). Further, considering the findings of Smith et al.,[19] the overall dependence of ISRM on salt concentration is considered as an indication of isolated salt molecule/polymer interactions in thin-film SPEs being more or less attractive than the intermolecular interactions of polymer chains. In particular, the reduction of ISRM at $x > 1$ and insignificant dependence of mass density, the latter implying volume expansion, on Li concentration in both bulk and confined thin-film SPEs (Fig. 6) suggest that the increase in Li-P and P-P coordination (Fig. 12) adversely affects the strength of salt/polymer interactions.

A further insight into the observed material properties may be gained by considering links between Li and PF_6 ion coordination and viscoelastic and electrochemical properties of confined thin-film and bulk SPEs. First, at concentrations $x < 0.5$, no significant $LiPF_6$ ion clustering in form of $Li_{n1}(PF_6)_n 2$ ($n1 \geq 1, n2 > 1$), which is attributed to Li-P and P-P coordination values of >1, is observed for the 60-Å-thick SPE film (Fig. 12). This is regarded as a contributing factor to a small increase in ISRM with respect to its value at $x = 0$ (Fig. 10). In contrast, in the bulk SPEs ion clustering initiates below $x = 0.5$, which is assumed to account partially for an absence of increase in bulk ISRM (Fig. 10). Furthermore, considering the similar coordination of PF_6 ions for the 60-Å-thick film and bulk SPEs at $x > 1$ (Fig. 12), it is concluded that the ion clustering behavior in this range of concentration is not significantly affected by the SPE film thickness. A further analogy with similar ISRM values for both structures at $x \geq 1$ is also observed (Fig. 10).

At variance with an approximately constant O-coordination of Li atoms in the bulk, at $x > 0.25$, a nonmonotonic reduction in the first three coordination-shells is observed for the 60-Å-thick SPE film (Fig. 13). Moreover, a significantly higher coordination in the first two shells with respect to the bulk is observed. The difference is seen as a result of a significantly higher salt dissociation with respect to the 380-Å-thick film and bulk SPEs (Fig. 14). However, we point out that a comparison of $Li(PF_6)_n$ group distributions for two interfacial area sizes of the 60-Å-thick SPE film with Li:O = 1:24 (Fig. 14) suggests that the obtained Li–P coordination at $x \leq 1$ for the smallest (1,000 $Å^2$) interfacial area may be subject to an underestimate due to the dispersion which results from the small size of the samples. The observed differences are found to be in agreement with the respective variance in ion distributions in terms of presence or absence of electric double layer (see the section "SPE Structure").

Mechanical Failure in Thin-Film SPE

From a molecular perspective, a higher failure stress value [Fig. 15(b)] is in agreement with a corresponding increase in number of dissociated $C–O_{ether}$ bonds at failure [Fig. 7(a)].

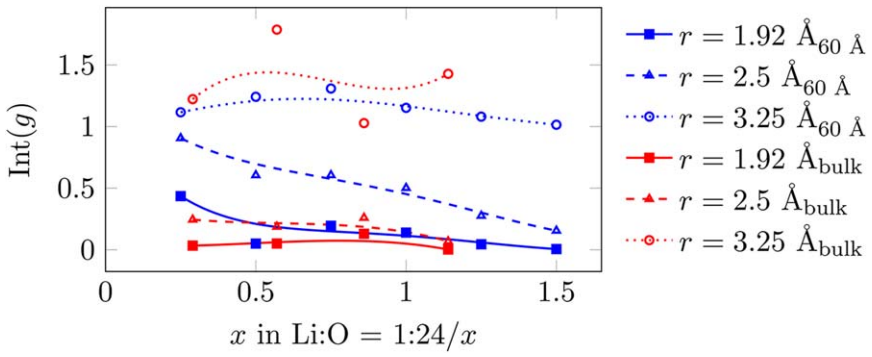

FIGURE 13 Dependence of Li—O first three coordination shells on $LiPF_6$ concentration for 60-Å-thick film and bulk SPEs. [Color figure can be viewed at wileyonlinelibrary.com]

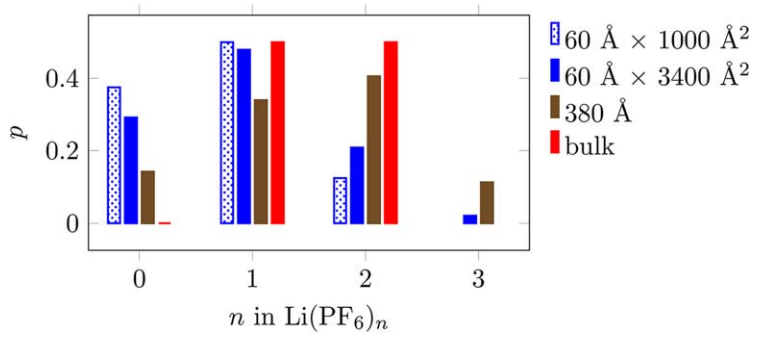

FIGURE 14 Dependence of Li—P first-shell-coordination distributions on SPE film thicknesses (p, probability, Li:O = 1:24/1:23/1:21 for the 60/380-Å-thick film and bulk SPEs, respectively). [Color figure can be viewed at wileyonlinelibrary.com]

Considering insignificant variation in initial density of interfacial C–O_{ether} bonds, the change is seen as a direct result of an increase in the largest principal strain at failure, with the salt-free structure taken as the reference state, due to the SPE-film thickness expansion (normal strain increase) and constant shear strain at failure. The conclusion is based on the assumption that, thereby, more chains are in stretched state prior to failure. The conclusion, however, does not account for the saturation in number of dissociated bonds at $x > 1$ (discussed below).

An increase in SPE thickness ($\approx 18\%$ for $x = 1.5$ compared to $x = 0$) implies less strain to make the chains taut for the same length of SPE polymer chains. Considering the findings of Stevens[8] regarding the strain that is required to stretch the minimum paths, a minimum path being defined as a zigzag (topological) path of minimum geometric length, connecting cross-linker attached to one fixed layer to another at the other fixed layer, as one of the main mechanical failure mechanisms at a bonded interface and insignificant change in shear strain at failure [considering the level of uncertainty according to Fig. 15(a)], we conclude that additional factors besides minimum paths through the network must influence the failure strain. Since the cited study reports only interfacial localization of bond failure, the shift in failure localization from the interface toward the electrolyte bulk at increasing the Li PF_6 concentration in this study [Fig. 7(b)] is seen as an indication of change in failure mechanism. The shift is attributed to a changing level of homogeneity in PF_6 ion distribution across the SPE film thickness, mainly due to the formation of electric double layer [Fig. 8(a,b)]. We also note that the saturation in number of dissociated bonds and reduction in failure localization at $x > 1$ are viewed as a second change in failure mechanism. Moreover, the coinciding reduction of ISRM (Fig. 10) precludes an increased contribution of viscosity to failure stress. Consequently, the change is attributed to a further expansion and increase of PF_6 concentration gradient at the interface [Fig. 8(b)], which accounts for a compatible expansion of gradient in mechanical properties of the material and to which a further increase in failure stress values is attributed [Fig. 15(b)].

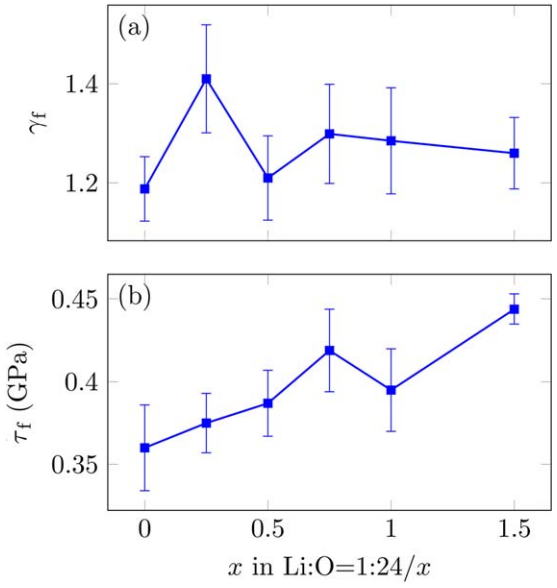

FIGURE 15 Dependence of shear failure (a) strain and (b) stress on $LiPF_6$ concentration for the 60-Å-thick SPE film. [Color figure can be viewed at wileyonlinelibrary.com]

Li Migration in Compressed State

No significant dependence of the free energy of Li-ion SPE-desolvation on uniaxial, interface-normal compression state is observed (Supporting Information, Fig. S7). Moreover, a comparison with the desolvation energies of Li ions in common organic liquid electrolytes (≈ 12 kcal/mol[49]) indicates an agreement with the estimated barriers of 10–15 kcal/mol (Supporting Information, Fig. S7) for the 60 Å SPE film. The value is obtained from the PMF difference for ion migration from 4–5 Å up to 2.5 Å distance from the GC surface, where the 2.5 Å distance corresponds to the estimated cutoff distance for Li/graphite interactions in vacuum.

SUMMARY

For thin-film (60 Å) SPE, insignificant variation of ISRM is observed within the experimentally used concentration range (Li:O≈1:20, $x \approx 1$). The observation is linked to insignificant

dependence of mass density on Li concentration for both thin-film and bulk SPEs. Similarly, no significant changes in the failure strain are obtained.

In contrast, an increasing strength with increasing salt concentration is predicted due to an increase in damage, based on bond dissociation, and failure stress estimates. Moreover, a nonmonotonic change in shear failure localization is observed. Both changes are interpreted as a result of a build-up of gradient-like material properties at interface due to the formation of an electric double layer at the interface and increasing salt concentration in the bulk-like part of the film.

No distinct dependence of ion distribution on electrolyte thickness is observed. At variance, differences in overall ion coordination, including the degree of salt dissociation (Fig. 14), with respect to bulk reference are found for thin-film SPE due to the electric double layer. The differences, however, are salt-concentration dependent, being the least significant at lower and upper limits of salt concentration. The differences are seen as a contributing factor to small variation in ISRM due to lithiation of the polymer.

A significant increase in mass density due to finite SPE-film thickness is seen. In particular, a partial phase change due to the increase in glass transition temperature has been identified for the thin-film SPE. The density increase is also considered as the cause for a higher mean value of ISRM compared to bulk SPE.

No significant change in SPE-desolvation energy is confirmed.

CONCLUSIONS

Considering the detected interdependencies of the mechanical properties and the atomic structure, a dependence of failure stress and failure localization on $LiPF_6$ ion concentration and distribution homogeneity is identified. Although the results correspond to high strain rate conditions (see the section "Simulation Settings and Ancillary Simulation Results"), compatible trends under quasi-static loading conditions can be predicted due to the monotonic change in relaxation moduli at $x > 0.5$ for thin-film SPE. Consequently, an optimum concentration with respect to viscoelastic and shear failure properties lies within the range $x \in (0.5, 1)$, which is compatible with the experimentally used value $x \approx 1$ for similar SPEs.

Furthermore, it is concluded that chemical interfacial bonding should be considered to improve the interfacial shear strength if microscopically smooth surfaces of amorphous carbon or graphitic particles constitute the electrode/SPE interface. Alternatively, the physical bonding between the respective material surfaces may be improved by forming O-containing surface-termination groups on the graphitic surface.

To identify optimum SPE film thickness, we assume that maximum strength properties can be linked to increased mass density, whereas for reduced ion transport distance, a minimum thickness of SPE is preferential. A limiting factor for the approach is attributed to the stability of SPE film with respect to its insulating property and avoidance of glass transition in SPE, which would imply a significant reduction in ionic transport due to the deactivation of segmental relaxation related mechanisms. Consequently, an optimum thickness for thin-film SPE element could be defined as the minimum thickness that preserves the rubber-like state of SPE in the considered range of operating temperatures.

Finally, we note that in this study, no modification of the potential was applied in relation to charging/discharging conditions. Therefore, polarization due to current flow was not accounted for and the current results represent an open circuit state. We assume, however, that, given the sizes of the double layer (<20 Å), shear failure zone (≤ 10 Å), and the localization of the failure zone (<40 Å), the effects of the closed circuit on the mechanical response of SPE films within ≈ 30 Å from the interface can be assumed as compatible with the present results at given mean concentrations of $LiPF_6$ in the respective layer.

ACKNOWLEDGMENTS

The research leading to these results has received funding from the European Research Council under the European Union's Seventh Framework Programme (FP7/2007–2013)/ERC Grant agreement n° 617972.

REFERENCES

1 L. E. Asp, S. Leijonmarck, T. Carlson, and G. Lindbergh, "Realisation of structural battery composite materials". *In: 20th International Conference on Composite Materials (Proceedings)* (**2015**).

2 K. K. Sairajan, G. S. Aglietti, K. M. Mani, *Acta Astronautica.* **2016**, *120*, 30.

3 B. Sun, D. Rehnlund, M. J. Lacey, D. Brandell, *Electrochim. Acta.* **2014**, *137*, 320.

4 N. S. Ergang, M. A. Fierke, Z. Wang, W. H. Smyrl, A. Stein, *J. Electrochem. Soc.* **2007**, *154*, A1135.

5 S. Leijonmarck, T. Carlson, G. Lindbergh, L. E. Asp, H. Maples, A. Bismarck, *Compos. Sci. Technol.* **2013**, *89*, 149.

6 S. Lee, J. Park, J. Yang, W. Lu, *Journal of the Electrochemical Society.* **2014**, *161*, A1218.

7 I. Hamerton, J. N. Hay, B. J. Howlin, J. R. Jones, S. Lu, *J. Mater. Chem.* **1998**, *8*, 1333.

8 M. J. Stevens, *Macromolecules* **2001**, *34*, 2710.

9 S. W. Sides, G. S. Grest, M. J. Stevens, *Macromolecules* **2002**, *35*, 566.

10 U. Kulmi, S. Basu, *Model. Simul. Mater. Sci. Eng.* **2006**, *14*, 1071.

11 J. Rottler, M. O. Robbins, *J. Adhes. Sci. Technol.* **2003**, *17*, 369.

12 D. Meng, S. K. Kumar, T. Ge, M. O. Robbins, G. S. Grest, *J. Chem. Phys.* **2016**, *145*, 094902.

13 H. Guk, D. Kim, S.-H. Choi, D. H. Chung, S. S. Han, *J. Electrochem. Soc.* **2016**, *163*, A917.

14 N.-S. Choi, Y. M. Lee, J. H. Park, J.-K. Park, *J. Power Sources* **2003**, *119–121*, 610–616. Selected papers presented at the 11th International Meeting on Lithium Batteries, pp 160.

15 F. Rahmani, M. Mahdavi, S. Nouranian, A. Al-Ostaz, *J. Polym. Sci. Part B: Polym. Phys.* **2017**, *55*, 1026.

16 H. Zhang, W. Li, *J. Reinf. Plast. Compos.* **2014**, *33*, 1520.

17 O. Borodin, G. D. Smith, R. L. Jaffe, *J. Comput. Chem.* **2001**, *22*, 641.

18 J. Karo, D. Brandell, *Solid State Ionics* **2009**, *180*, 1272.

19 G. D. Smith, D. Bedrov, L. Li, O. Byutner, *J. Chem. Phys.* **2002**, *117*, 9478.

20 L. E. Asp, E. S. Greenhalgh, *Compos. Sci. Technol.* **2014**, *101*, 41.

21 T. Davris, A. V. Lyulin, *J. Chem. Phys.* **2015**, *143*, 074906.

22 O. Verners, B. J. Thijsse, A. C. T. van Duin, A. Simone, *Electrochim. Acta* **2016**, *221*, 115.

23 Sigma-Aldrich Co. LLC. *Online Product Catalog*. http://www.sigmaaldrich.com/technical-service-home/product-catalog.html. Accessed 2015-3-20. **2015**.

24 R. De Lisi, G. Lazzara, S. Milioto, *Phys. Chem. Chem. Phys.* **2011**, *13*, 12571.

25 B. Sun, C. Xu, J. Mindemark, T. Gustafsson, K. Edstrom, D. Brandell, *J. Mater. Chem. A* **2015**, *3*, 13994.

26 A. Márquez, P. B. Balbuena, *J. Electrochem. Soc.* **2001**, *148*, A624.

27 A. Márquez, *Mater. Chem. Phys.* **2007**, *104*, 199.

28 M. M. S. Dwaikat, C. Spitas, V. Spitas, *Compos. B Eng.* **2013**, *44*, 501.

29 D. R. Dreyer, S. Park, C. W. Bielawski, R. S. Ruoff, *Chem. Soc. Rev.* **2010**, *39*, 228.

30 S. Plimpton, *J. Comput. Phys.* **1995**, *117*, 1.

31 H. M. Aktulga, J. C. Fogarty, S. A. Pandit, A. Y. Grama, *Parallel Comput.* **2012**, *38*, 245.

32 A. C. T. van Duin, S. Dasgupta, F. Lorant, W. A. Goddard, *J. Phys. Chem. A* **2001**, *105*, 9396.

33 A. K. Rappe, W. A. Goddard, *J. Phys. Chem.* **1991**, *95*, 3358.

34 M. M. Islam, V. S. Bryantsev, A. C. T. van Duin, *J. Electrochem. Soc.* **2014**, *161*, E3009.

35 M. T. Ong, O. Verners, E. W. Draeger, A. C. T. van Duin, V. Lordi, J. E. Pask, *J. Phys. Chem. B* **2015**, *119*, 1535.

36 S. Chaurasia, R. Singh, S. Chandra, *Vibrat. Spectrosc.* **2013**, *68*, 190.

37 *LAMMPS Documentation*. http://lammps.sandia.gov/doc/Manual.html. Accessed 2017-04-26. **2015**.

38 M. E. Tuckerman, J. Alejandre, R. López-Rendón, A. L. Jochim, G. J. Martyna, *J. Phys. A Math. Gen.* **2006**, *39*, 5629.

39 G. J. Martyna, D. J. Tobias, M. L. Klein, *J. Chem. Phys.* **1994**, *101*, 4177.

40 G. J. Martyna, M. L. Klein, M. Tuckerman, *J. Chem. Phys.* **1992**, *97*, 2635.

41 G. Malucelli, G. Gozzelino, F. Ferrero, R. Bongiovanni, A. Priola, *J. Appl. Polym. Sci.* **1997**, *65*, 491.

42 R. D. Raharjo, H. Lin, D. F. Sanders, B. D. Freeman, S. Kalakkunnath, D. S. Kalika, *J. Membr. Sci.* **2006**, *283*, 253.

43 D. Frenkel, B. Smit, *Understanding Molecular Simulation: From Algorithms to Applications*. Academic Press, **1996**.

44 G. Fiorin, J. Hénin, and A. Kohlmeyer, *Collective variables module reference manual for LAMMPS*. http://lammps.sandia.gov/doc/PDF/colvars-refman-lammps.pdf. Accessed 2015-09-03. **2015**.

45 D. Diddens, A. Heuer, O. Borodin, *Macromolecules* **2010**, *43*, 2028.

46 A. Stukowski, *Model. Simul. Mater. Sci. Eng.* **2010**, *18*, 015012.

47 D. V. Guseva, P. V. Komarov, A. V. Lyulin, *J. Chem. Phys.* **2014**, *140*, 114903.

48 T. Kawai, *Jpn. J. Appl. Phys.* **2013**, *52*, 04CN08.

49 K. Xu, A. von Wald Cresce, *J. Mater. Res.* **2012**, *27*, 2327.